Available online at www.sciencedirect.com
ScienceDirect
Trans. Nonferrous Met. Soc. China 35(2025) 2954−2968
Transactions of Nonferrous Metals Society of China
www.tnmsc.cn

Diffusion bonding of high Nb β/γ-TiAl intermetallics to Ni-based superalloy using Ti interlayer under pulse current

Lai-qi ZHANG[1#], Kun HE[1#], Qiang GAO[1,2]

1. State Key Laboratory for Advanced Metals and Materials, University of Science and Technology Beijing, Beijing 100083, China;
2. Branch of Vanadium and Titanium Research Institute, Ansteel Beijing Research Institute Co., LTD., Beijing 102209, China

Received 22 January 2024; accepted 2 September 2024

Abstract: High Nb β/γ-TiAl (HNBG) intermetallics and Ni-based superalloy (IN718) were diffusion-bonded using pure Ti foil interlayer under pulse current. The microstructure, element segregation, and mechanical properties of HNBG/Ti/IN718 joint were investigated. The effect of Ti interlayer on microstructure and mechanical properties of the joint was discussed. The typical microstructure of HNBG/Ti/IN718 joint was HNBG//$\beta/B2$, τ_3-$NiAl_3Ti_2$//α_2-Ti_3Al//α-Ti+δ-$NiTi_2$, β-Ti//δ-$NiTi_2$//β_2-(Ni,Fe)Ti//Cr/Fe-rich η-Ni_3Ti, η-Ni_3Ti, α-Cr, δ-Ni_3Nb//η-Ni_3Ti, γ-Ni, δ-Ni_3Nb//IN718. The gaps and Kirkendall voids exhibited a gradual disappearance with increasing bonding temperature. The mechanism of Cr, Fe and Nb elements segregation was that NiTi phase hindered the diffusion of them. The nano-indentation results demonstrated that diffusion zones on IN718 alloy side had higher hardness. The maximum shear strength of the joint (326 MPa) was achieved at bonding parameters of 850 °C, 20 min and 10 MPa. The fracture occurred in Zones IV and V, and the fracture modes were brittle fracture and cleavage fracture. The introduction of Ti interlayer resulted in improved microstructure and enhanced bonding strength of the joint.

Key words: high niobium β/γ-TiAl intermetallics; IN718 alloy; Ti interlayer; diffusion bonding; microstructure; mechanical properties; element segregation

1 Introduction

TiAl alloys have become one of the most promising high-temperature structural materials in the aerospace industry due to their low density, high specific strength, excellent creep resistance, and high-temperature oxidation resistance [1−5]. High niobium β/γ-TiAl (HNBG) alloy with excellent high-temperature deformation ability has been produced by our research team, and its forging without a can has also been achieved [6]. Furthermore, its welding with dissimilar materials is unavoidable in engineering applications. IN718 alloy is the most widely used superalloy with excellent high-temperature strength, good oxidation resistance, and weldability [7−9]. Therefore, to promote the practical engineering application of high niobium β/γ-TiAl, it is of great significance to investigate the joining of HNBG to IN718 alloys.

TiAl alloys are not suitable for fusion welding due to their crack susceptibility [10,11]. In recent years, brazing and diffusion bonding methods to join TiAl and Ni-based alloys have garnered considerable attention. SEQUEIROS et al [12] successfully achieved brazed joining of γ-TiAl to

[#] Lai-qi ZHANG and Kun HE contributed equally to this work

Corresponding author: Lai-qi ZHANG, Tel: +86-10-62334925, E-mail: zhanglq@ustb.edu.cn

https://doi.org/10.1016/S1003-6326(25)66859-2

1003-6326/© 2025 The Nonferrous Metals Society of China. Published by Elsevier Ltd & Science Press
This is an open access article under the CC BY-NC-ND license (http://creativecommons.org/licenses/by-nc-nd/4.0/)

IN718 alloys by using Ag−Cu−In−Ti filler, but the formation of brittle compounds $AlCu_2Ti$ and $AlNi_2Ti$ limited shear strength to only 228 MPa. REN et al [13] effectively brazed Ti_3Al-based and Ni-based alloys (GH536) using Ag−Cu−Pd brazing filler, yet Ag-based filler did not meet high-temperature demands and was costly. Furthermore, DONG et al [14] utilized amorphous Cu−Ti−Zr−Ni filler to braze TiAl and Ni-based alloys (GH4169), reducing costs but adversely affecting the mechanical properties due to the formation of excess brittle intermetallics. LI et al [15] notably brazed TiAl to Ni-based alloys (GH99) using Ti foil as filler, reducing costs and emphasizing the impact of microstructure on joint strength. In summary, these researches indicated the potential yet significant limit for brazing TiAl and Ni-based alloys, primarily due to brazing material selection, thickening of the interfacial reaction layer, and high weld brittleness. Contrastingly, due to the high accuracy and lower residual stresses, diffusion bonding was regarded as the preferred method for joining TiAl alloys with dissimilar materials. However, research focusing on diffusion bonding of TiAl to nickel-based alloys remains scarce. ROMOS et al [16] joined TiAl and IN718 alloys using nano-Ni/Al interlayer via conventional hot pressing diffusion bonding technique. However, the cost of preparing the interlayer by magnetron sputtering was high. LUO et al [17] and LI et al [18] directly joined TiAl with Ni-based alloys through conventional hot pressure diffusion bonding (carried out on a Gleeble) combined with laser surface modification, respectively. However, the surface modification increased the number of steps in entire process. Furthermore, diffusion bonding using hot pressing method is usually time-consuming. In contrast, spark plasma sintering (SPS) joining is a novel solid diffusion bonding technique. The electrical migration effect during the SPS process can significantly enhance the capability of atomic diffusion, effectively reducing bonding temperatures and time, thus greatly improving the efficiency. Considering its advantages, GAO et al [19] conducted a preliminary investigation into the application potential of SPS technique in diffusion bonding, and successfully achieved highly efficient diffusion bonding of HNBG to IN718 alloys without relying on interlayers.

In our previous research, the composition transition was abrupt in HNBG/IN718 joints, which were continuously distributed with a large number of Ti−Ni−Al brittle compounds [19]. In order to further improve the microstructure and strengthen the bonding strength of the joint, a novel approach to incorporating Ti interlayer was proposed in this work. The effect of bonding temperature on the microstructure and mechanical properties was investigated. The mechanism of element segregation was revealed by utilizing first-principles calculations. Moreover, the diffusion bonding and fracture mechanisms were also investigated, respectively.

2 Experiment and calculation

2.1 Experimental procedure

The HNBG alloy was produced by vacuum levitation melting with the nominal composition of Ti−44Al−8Nb−1.5Mn−1.0Cr−0.2B−0.2Y (at.%); Subsequently, it was used as a welding matrix after being annealed at 1150 °C for 24 h. The microstructure of HNBG alloy was shown in detail in our previous study [20], which mainly consists of dark-gray γ and light-gray $\beta/B2$ phases dotted with TiB_2 and Y_2O_3 phases. IN718 alloy was synthesized in situ from alloy powders by SPS sintering (1210 °C, 15 min, 50 MPa) and the nominal composition is shown in Table 1. Its microstructure after solution ((950 °C, 1 h) + WQ) and aging ((720 °C, 8 h) + (620 °C, 8 h) + AC) treatment is shown in Fig. 1, which is mainly composed of γ-Ni and δ-Ni_3Nb phases [19]. In addition, pure Ti foil consists of equiaxed α-Ti and α-Ti with twin structures.

HNBG and IN718 alloys were cut into dimensions of 30 mm × 30 mm × 3.5 mm and 28 mm × 28 mm × 3.5 mm, respectively, and the mating surface was ground on SiC abrasive papers. Pure Ti foil was thinned to (30±10) μm and then used as an interlayer. All samples were ultrasonically cleaned with alcohol for 20 min. The Ti foil was placed between the HNBG and IN718

Table 1 Chemical composition of IN718 alloy (wt.%)

Ni	Cr	Mo	Mn	Si	Nb
53	19	3.3	0.35	0.35	5.1
Cu	Co	Ti	Al	C	Fe
0.3	1.0	1.15	0.8	0.08	Bal.

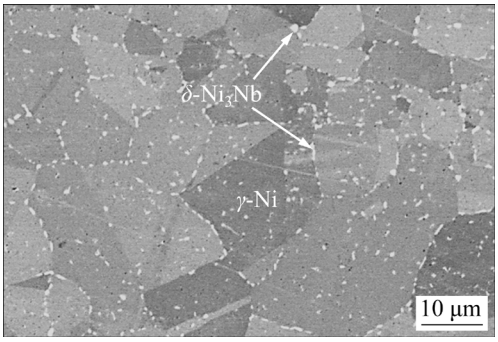

Fig. 1 Microstructure of IN718 alloy after solution and aging treatment

samples to form as an integrated sandwich structure; Subsequently, it was placed into a mold for diffusion bonding. The SPS device had an output current range of 0−10 kA. The bonding temperature ranged from 750 to 900 °C, and bonding time was varied from 10 to 30 min with the bonding pressure of 10 MPa. The vacuum degree and heating rate during diffusion bonding were 5×10^{-2} Pa and 100 °C/min, respectively.

The microstructure of the joints was characterized by employing a scanning electron microscope (SEM, Zeiss SUPRA−55) equipped with an energy dispersive spectroscope (EDS) and an electron backscatter diffraction (EBSD) system. The samples for EBSD test were ground to 5000-grit SiC abrasive paper, followed by diamond polishing, and subsequently polished on the polymer synthetic cloth using a mixture of 0.05 μm silica suspension and hydrogen peroxide (volume ratio: 3:1) for 1 h. The hardness of the phases in the joint was measured using nano-indentation with a load of 20 mN. The shear strength test was performed with a shear area of 4 mm × 4 mm at an indenter travel rate of 0.5 mm/min.

2.2 Modeling and parameters setting

The crystal structure of the NiTi phase with space group of $P2_1/m$ and lattice constants of a=4.005 Å, b=2.915 Å, c=4.754 Å, α=79.068°, β=90.000° and γ=90.999°, as shown in Fig. 2(a). The Ni and Ti atoms in the primitive cell were located at 2e (0.2164, 0.2500, 0.4167) and 2e (0.6752, 0.2500, 0.0372), respectively, and the site occupation factors (SOF) of Ni and Ti atoms were both 1. The crystal structures of 2×2×5 supercell doped with Cr or Fe atoms and 2×2×5 supercell doped with Nb atoms are shown in Figs. 2(b) and (c), respectively, where Cr and Fe atoms occupied Ni sites, and Nb atoms occupied Ti sites. The model was constructed by Materials Studio, and the calculations were implemented using the Vienna Ab-Initio Simulation Package (VASP) based on density functional theory. The electron exchange-correlation interactions were calculated by the Perdew−Burke−Ernzerhof (PBE) function in the generalized gradient approximation (GGA) via the projector augmented wave (PAW) method. The first Brillouin zone was sampled using the Monkhorst-Pack 9×9×9 special k-point grid method and the cut-off energy was 520 eV.

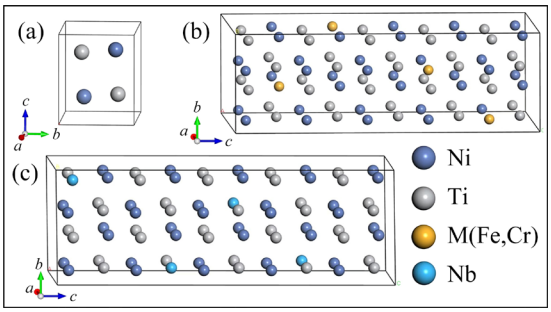

Fig. 2 Primitive cell of β_2-NiTi and supercell of β_2-NiTi doped with different elements: (a) Primitive cell; (b) 2×2×5 supercell doped with Cr or Fe atoms; (c) 2×2×5 supercell doped with Nb atoms

3 Result and discussion

3.1 Typical microstructure characteristics of HNBG/Ti/IN718 joint

Figure 3 illustrates the typical microstructure of HNBG/Ti/IN718 joint obtained at 850 °C, 20 min and 10 MPa. The joint was divided into seven zones (labeled as Zones I to VII) from HNBG to IN718 alloys based on morphological characteristics. The elemental composition of phases is shown in Table 2. At HNBG/Ti interface, Zone I consisted of bright-gray phase at Spot A and short rod-like phase at Spot B, as seen in Fig. 3(b). The phase at Spot A was primarily composed of Ti, Al, and Nb elements, the composition of which was close to that of $\beta/B2$ phase [19]. The morphology and composition of phase at Spot B were similar to those of τ_3-$NiAl_3Ti_2$ phase in HNBG/IN718 joint [19]. Moreover, phases at Spots A and B were indexed as $B2$ and α_2-Ti_3Al phases by EBSD, respectively, as illustrated in Fig. 4(c). The α_2 ($D0_{19}$) and τ_3 (C14) phases belonged to the same space

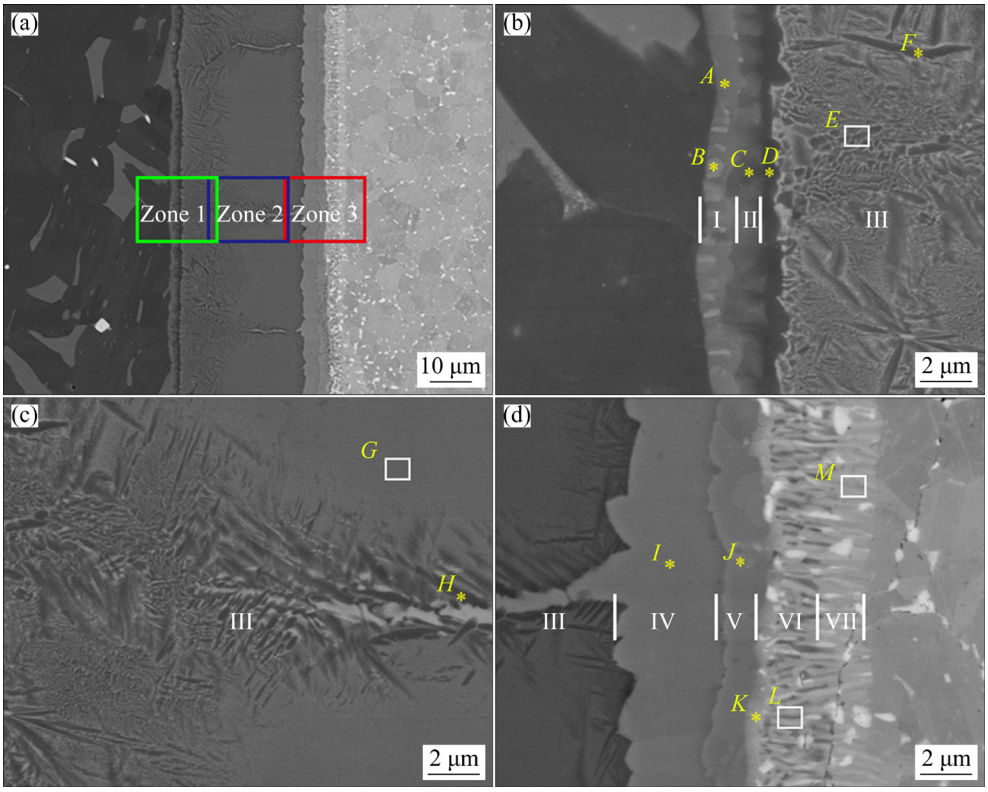

Fig. 3 Typical microstructure of HNBG/Ti/IN718 joint at 850 °C, 20 min and 10 MPa: (a) BSE image; (b) Enlarged image of Zone 1 in (a); (c) Enlarged image of Zone 2 in (a); (d) Enlarged image of Zone 3 in (a)

Table 2 Element contents at spots marked in Fig. 3 detected by EDS

Spot	Content/at.%							Possible phase
	Ti	Al	Ni	Cr	Fe	Nb	Mn	
A	58.68	28.40	2.66	0.78	0.43	8.06	0.99	$\beta/B2$
B	44.52	35.93	11.27	–	–	8.28	–	τ_3-$NiAl_3Ti_2$
C	67.90	25.42	0.48	0.25	–	5.95	–	α_2-Ti_3Al
D	84.20	12.64	1.38	–	–	1.78	–	α-Ti
E	77.55	12.28	5.59	0.37	1.45	2.75	–	α-Ti+δ-$NiTi_2$
F	84.75	10.86	1.73	0.32	0.74	1.60	–	α-Ti
G	82.76	6.93	6.43	0.70	2.22	0.96	–	β-Ti
H	88.44	6.03	2.85	0.73	1.12	0.82	–	α-Ti
I	66.09	0.33	28.02	–	5.06	–	–	δ-$NiTi_2$
J	47.75	0.37	32.91	1.86	16.73	0.26	0.11	β_2-(Ni,Fe)Ti
K	23.19	0.68	18.27	25.64	27.40	4.79	0.36	Cr/Fe-rich η-Ni_3Ti
L	14.46	1.29	50.41	23.04	8.04	2.77	–	η-Ni_3Ti+α-Cr
M	8.31	2.04	44.81	26.20	18.65	–	–	η-Ni_3Ti+γ-Ni

group ($P6_3/mmc$). Therefore, combining EDS and EBSD, phases at Spots *A* and *B* were identified as *B*2 and τ_3-$NiAl_3Ti_2$ phases, respectively. Furthermore, the original $\beta/B2$ phase initially existed in HNBG alloy, which did not satisfy the K−S orientation relationship with γ-TiAl phase, as illustrated in Fig. 4(b). Conversely, the $\beta/B2$ phase newly formed in bonding process satisfied the K−S orientation with γ-TiAl phase, as illustrated in Fig. 4(d). Consequently, it was indicated that some

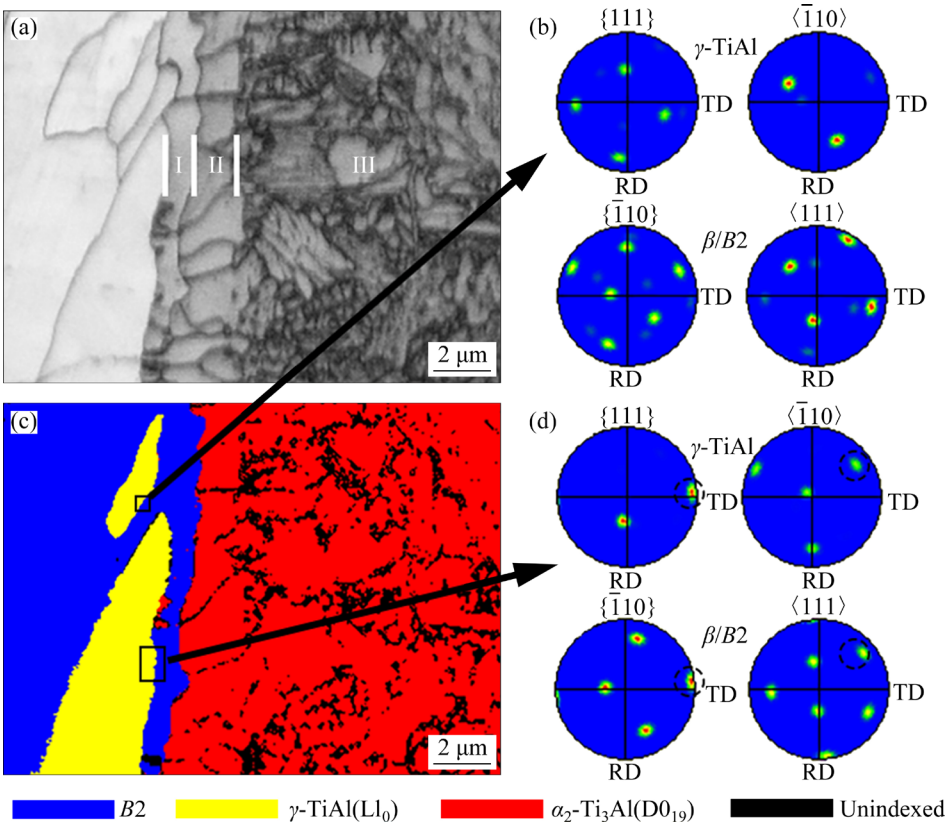

Fig. 4 EBSD characterization results of Zones I−III in joint obtained at 850 °C, 20 min and 10 MPa: (a) Band contrast map; (b, d) Polar figures; (c) Phase distribution map

γ-TiAl phase transformed into $\beta/B2$ phase during joining process. Zone II had a single phase at Spot *C*, which was primarily composed of the Ti, Al and Nb elements with Ti/Al molar ratio ranging between 2 and 3. Consequently, the phase at Spot C was inferred to be α_2-Ti_3Al phase by the Ti−Al−Nb system [21]. Furthermore, the related research indicated that α_2-Ti_3Al phase easily formed on the side of τ_3-$NiAl_3Ti_2$ phase [22]. Combined with the phase map in Fig. 4(c), the phase at Spot *C* was further identified as α_2-Ti_3Al phase. In our previous research, the HNBG/IN718 joint produced by direct diffusion bonding contained a great amount of τ_3-$NiAl_3Ti_2$ and τ_4-Ni_2AlTi phases [19]. In this work, Ti interlayer increased the diffusion distance for Ni atoms, thereby significantly reducing the amount of Ni atoms that diffused from IN718 to HNBG alloys. Consequently, the formation of the τ_3-$NiAl_3Ti_2$ and τ_4-Ni_2AlTi phases was significantly reduced in IN718/Ti/HNBG joint. Instead, a small amount of α_2 phase with lower brittleness was formed. Therefore, the introduction of Ti interlayer reduced the formation of brittle compounds on the HNBG side of the joint, which may contribute to enhancing the bonding strength of the joint.

In Ti interlayer, the part of Zone III near HNBG alloy side included the phase at Spot *D*, the point-like structure at Spot *E* and the needle-like phase at Spot *F*, as illustrated in Fig. 3(b). Phases at Spots *D* and *F* were mainly composed of Ti elements, which were indexed as α_2-Ti_3Al phase by EBSD, as depicted in Fig. 4(c). The α-Ti and α_2-Ti_3Al have the same crystal structure (HCP) with close lattice parameters. Consequently, both phases at Spots *D* and *F* were identified as α-Ti phase by combining EDS and EBSD analysis. The phase at Spot *E* was the obvious eutectoid structure (α-Ti + δ-$NiTi_2$) [23]. This obvious eutectoid structure was formed through the eutectoid reaction of β-Ti→ α-Ti + δ-$NiTi_2$ during the cooling stage, according to Ti−Ni phase diagram in Fig. 5 [24]. The part of Zone III near IN718 alloy side consisted of the eutectoid structure (α-Ti + δ-$NiTi_2$), the phase at Spot *G* and needle-like phase at Spot *H*, as illustrated in Fig. 3(c). The phases at Spots *G* and *H* were primarily composed of Ti element, with a particularly high content of Ti in the phase at Spot *H* (88.44 at.%). Furthermore, combined with the

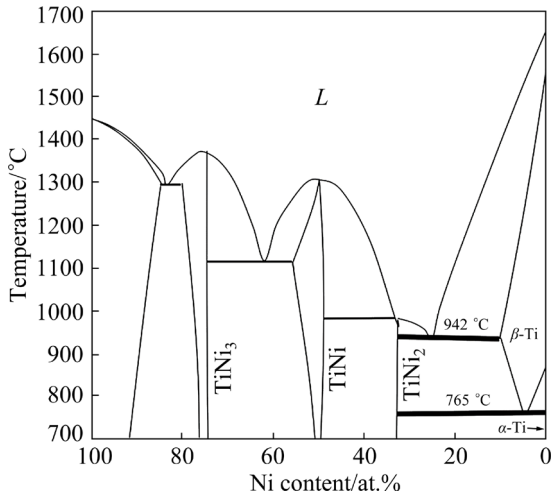

Fig. 5 Ti−Ni binary phase diagram [24]

phase distribution map in Fig. 6(b), phases at Spots *G* and *H* could be identified as β-Ti and α-Ti phases, respectively. In comparison to the HNBG/IN718 joint obtained by direct diffusion bonding in our previous research [19], the β-Ti phase with relatively good plasticity was formed in the Ti interlayer in this work. This could help to alleviate residual stresses and increase the shear strength of the joint.

At Ti/IN718 interface, Zone IV had a single phase, which was mainly composed of Ti and Ni elements with a molar ratio of approximately 2:1. Furthermore, the phase at Spot *I* was further identified as δ-$NiTi_2$ phase in combination with phase map in Fig. 7(b). Zone V also had a single phase (at Spot *J*), which was primarily composed of Ti, Ni and Fe elements, and molar ratio of Ti to the total of Ni and Fe was close to 1:1. Furthermore, the phase at Spot *J* was indexed as β_2-NiTi phase. Therefore, combining EDS and EBSD analysis, the phase at Spot *J* was confirmed to be the β_2-(Ni,Fe)Ti phase. Zone VI comprised phases at Spots *K* and *L*, as illustrated in Fig. 3(d). The phase at Spot *K* was mainly composed of Ti, Fe, Cr and Ni elements with the molar ratio of Ti to the total of Fe, Cr and Ni being close to 1:3. Furthermore, the phase at Spot *K* was indexed as α_2-Ti_3Al phase, as depicted in Fig. 7(b). The α_2-Ti_3Al and η-Ni_3Ti

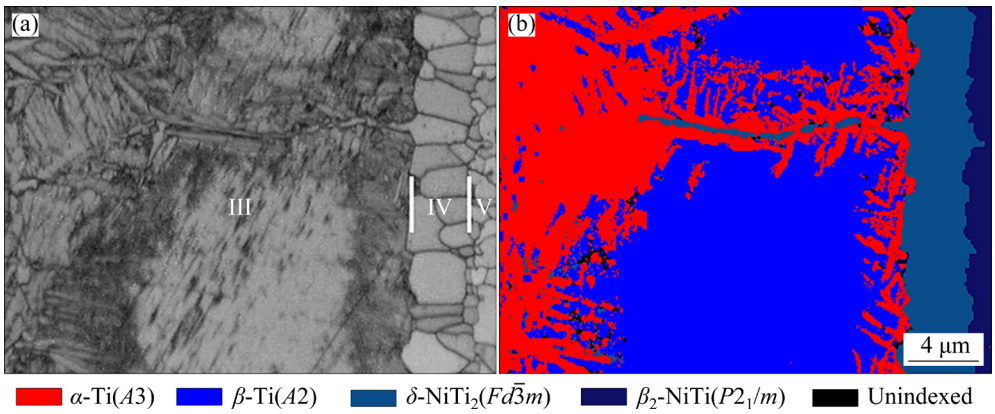

Fig. 6 EBSD characterization results of Zones III−V in joint obtained at 850 °C, 20 min and 10 MPa: (a) Band contrast map; (b) Phase distribution map

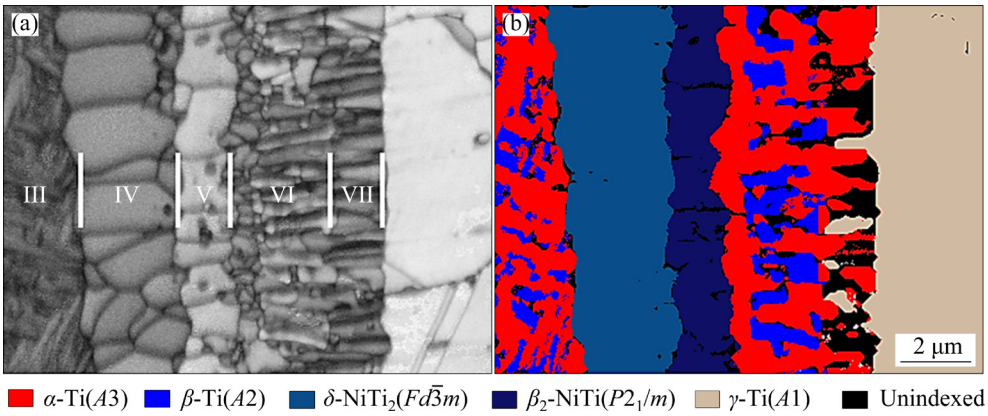

Fig. 7 EBSD characterization results of Zones III−VII in joint obtained at 850 °C, 20 min and 10 MPa: (a) Band contrast map; (b) Phase distribution map

phases belong to the same space group ($P6_3/mmc$). Consequently, the phase at Spot K was determined to be the Cr/Fe-rich η-Ni_3Ti phase by combining EDS and EBSD analysis. Spot L consisted of alternately distributed black-gray and bright-gray phases. Due to the small size of the phases, EDS analysis was carried out for them together. The phases were primarily composed of Ti, Ni and Cr elements with a molar ratio of Ti to Ni being close to 1:3 and a high content of Cr. Therefore, the black-gray and bright-gray phases were inferred to be α-Cr and η-Ni_3Ti phases, respectively. Furthermore, the black-gray phase was indexed as β-Ti phase. The β-Ti and α-Cr phases belong to the same space group ($Im\overline{3}m$). Therefore, the black-gray phase was confirmed to be α-Cr phase in combination with EDS and EBSD. The bright-gray phase was identified as η-Ni_3Ti phase by comparing its contrast with that of the Cr/Fe-rich η-Ni_3Ti phase. Moreover, some white δ-Ni_3Nb phases were also found in Zone VI. The phases in Zone VII was identified as γ-Ni, η-Ni_3Ti and δ-Ni_3Nb phases through the integration of BSE, EDS and EBSD analysis.

According to analysis above, the typical microstructure of the HNBG/Ti/IN718 joint was HNBG//β/$B2$, τ_3-$NiAl_3Ti_2$//α_2-Ti_3Al//α-Ti+δ-$NiTi_2$, β-Ti//δ-$NiTi_2$//β_2-(Ni,Fe)Ti//Cr/Fe-rich η-Ni_3Ti, η-Ni_3Ti, α-Cr, δ-Ni_3Nb//η-Ni_3Ti, γ-Ni, δ-Ni_3Nb//IN718. The introduction of the Ti interlayer significantly reduced the formation of Ti−Ni−Al ternary brittle intermetallics, and the β-Ti phases with relatively good plasticity were formed within Ti interlayer.

3.2 Mechanism of element segregation in joint

The element distribution on the IN718 alloy side is illustrated in Fig. 8. The Cr/Fe-rich η-Ni_3Ti phase in Zone VI exhibited the most pronounced disparity in element distribution, which was characterized by a relative deficiency in Ni element and a relative enrichment in Cr, Fe and Nb elements.

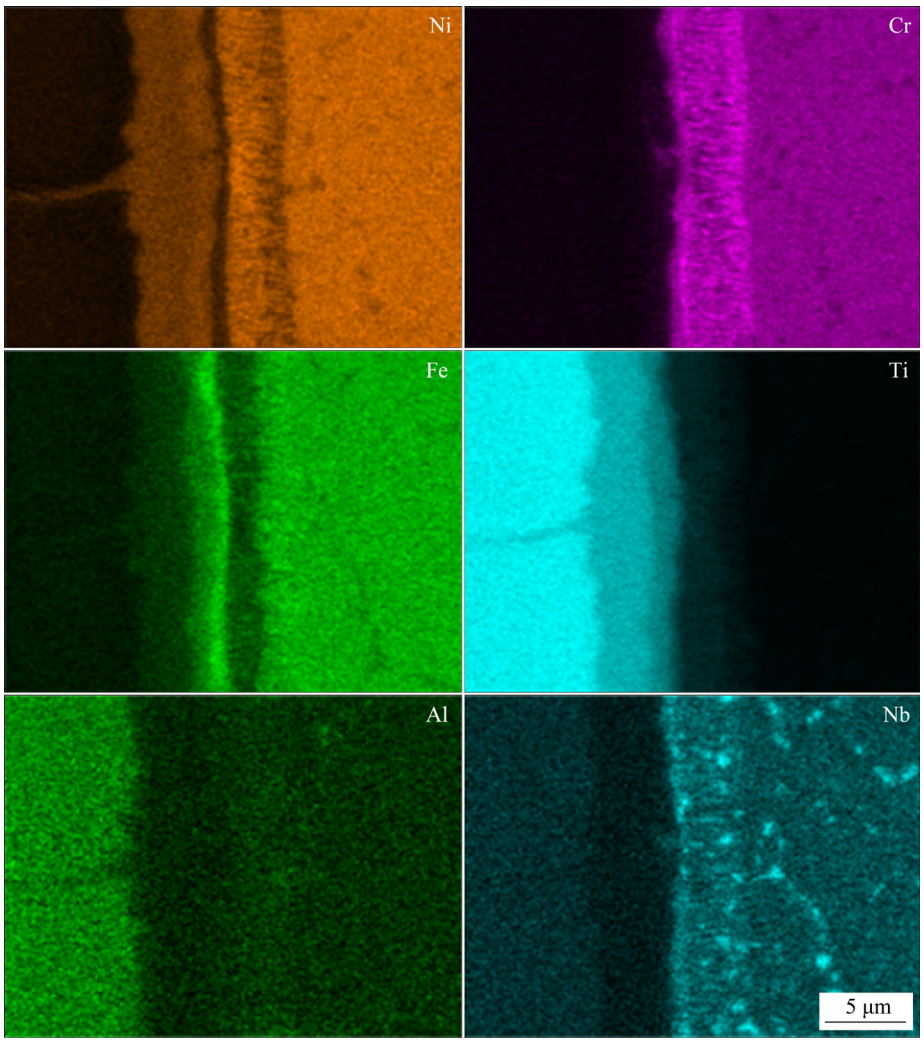

Fig. 8 Element distribution on IN718 alloy side in HNBG/Ti/HNBG joint

Due to the high affinity between Ti and Ni elements [25], a large number of Ni atoms diffused into Ti interlayer. Furthermore, the η-Ni_3Ti phase was first formed at the original interface between the Ti interlayer and IN718 alloy [26]. Consequently, the deficiency in Ni element occurred in Cr/Fe-rich η-Ni_3Ti phase during the subsequent bonding process.

Regarding the enrichment of Cr, Fe and Nb elements in Zone VI, it was further analyzed by considering the formation energy of NiTi phase and its doped phases with Cr, Fe and Nb atoms, respectively. The formation energy of the phases was calculated by first-principles calculations as follows:

$$\Delta E_f=(E_{Ni_xTi_y}-xE_{Ni}-yE_{Ti})/(x+y)$$

where ΔE_f is the formation energy of NiTi phases doped with Cr, Fe and Nb atoms, respectively; $E_{Ni_xTi_y}$ is the total energy of NiTi phase; E_{Ni} and E_{Ti} are the energy of a single Ni and Ti atom, respectively; x and y are the numbers of Ni and Ti atoms, respectively.

It can be seen from Fig. 9 that the doping of Cr, Fe and Nb atoms increased the formation energy of NiTi phase, with Cr exhibiting the most pronounced effect. Consequently, NiTi phase hindered the diffusion of Cr, Fe and Nb atoms with the significant obstruction for Cr.

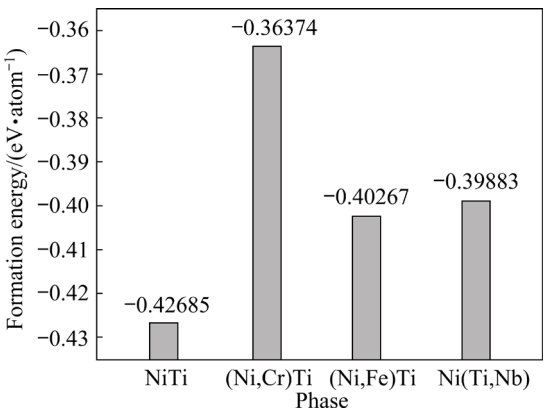

Fig. 9 Formation energy of NiTi phase and its doped phases with Cr, Fe and Nb atoms

3.3 Effect of bonding temperature on microstructure of HNBG/Ti/IN718 joint

Figure 10 illustrates the microstructure of HNBG/Ti/IN718 joint obtained at different bonding temperatures. It can be observed that there were Kirkendall voids present in Zones II, VI and VII at 750 °C (Fig. 10(b)). This was because different kinds of atoms have different diffusion rates [27]. Concurrently, the gaps with larger sizes were observed at the interface between Zones IV and V due to insufficient diffusion of elements. As illustrated in Fig. 10(e), the Kirkendall voids disappeared at 800 °C, while smaller voids remained along the interface between Zones IV and V. As the bonding temperature further increased, a defect-free joint was achieved at 850 °C (Fig. 3(a)).

When the bonding temperature was 750 °C, Zone I was not observed in Fig. 10(a) due to the limited resolution of the BSE image. However, Zone I can be observed in the band contrast map of Fig. 11(a). It can be seen from Fig. 10(d) that Zone I only had $\beta/B2$ phase but no τ_3-$NiAl_3Ti_2$ phase at 800 °C. As the bonding temperature increased to 850 °C, the diffusion capacity of Ni atoms was enhanced. Consequently, the oversaturation of Ni atoms in $\beta/B2$ phase occurred when γ-TiAl phase transformed into $\beta/B2$ phase, which led to the precipitation of τ_3-$NiAl_3Ti_2$ from $\beta/B2$ phase. The size of τ_3-$NiAl_3Ti_2$ phase increased at 900 °C, as illustrated in Fig. 10(g).

Zone II exhibited a unique characteristic distinct from other zones, and the thickness of which gradually decreased with rising bonding temperature. This phenomenon can be attributed to two key factors. On the one hand, the critical Al content required for the transformation from α-Ti to α_2-Ti_3Al increased as the temperature rose [28]. On the other hand, the resistance to α_2-Ti_3Al grain boundary migration increased due to the diffusion of more β-phase stabilizing elements into Ti interlayer with increasing bonding temperature. Furthermore, it can be seen from Fig. 11 that α_2-Ti_3Al grains tended to merge and grow in the direction perpendicular to the diffusion layer as the temperature increased. When the temperature was 900 °C, the size of α_2-Ti_3Al grains in the direction perpendicular to diffusion layer was significantly larger than that in the direction parallel to the diffusion layer.

Within Zone III, the proportion of β-Ti phase gradually increased with rising temperature. The phenomenon can be attributed to the augmented diffusion of β-phase stabilizing elements into Ti interlayer with rising temperature. Consequently, more β-Ti phases can be retained until room temperature. Additionally, the extension distance of

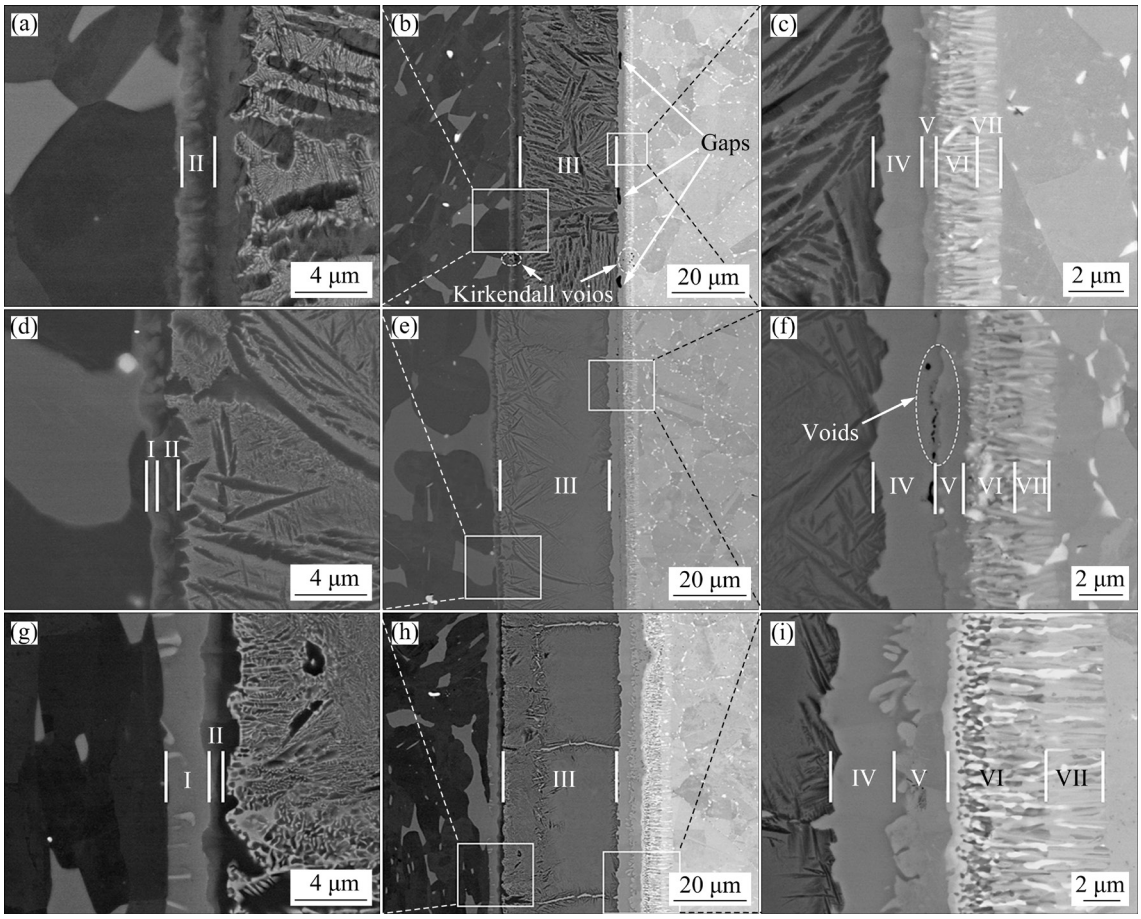

Fig. 10 Effect of bonding temperature on microstructure of HNBG/Ti/IN718 joints at 10 min and 10 MPa: (b) 750 °C; (e) 800 °C; (h) 900 °C; (a, c) Local amplification of (b); (d, f) Local amplification of (e); (g, i) Local amplification of (h)

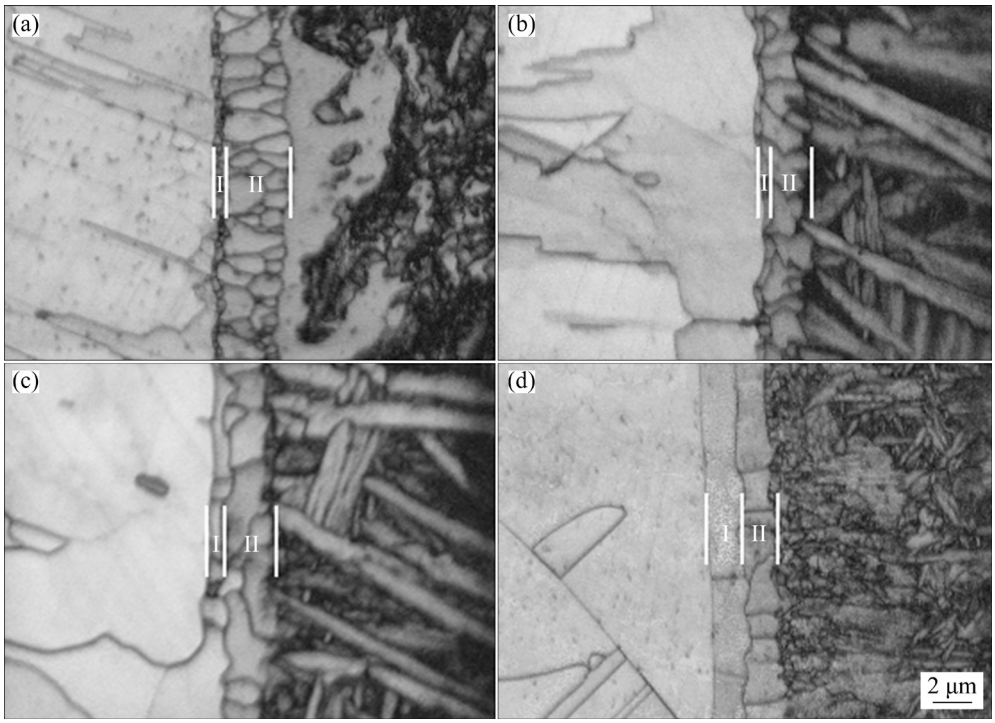

Fig. 11 Band contrast maps of HNBG alloy side in HNBG/Ti/IN718 joints at 10 min, 10 MPa and different bonding temperatures: (a) 750 °C; (b) 800 °C; (c) 850 °C; (d) 900 °C

δ-$NiTi_2$ phase in Zone III increased as the temperature rose. Zone VI was mainly characterized by an augmented content of α-Cr phase, which was attributed to an elevated Cr enrichment degree with rising temperature.

3.4 Diffusion bonding mechanism of HNBG/Ti/IN718 joint

The phase transformation at HNBG/Ti interface was simpler. The transformation from γ-TiAl to $\beta/B2$ phases and the precipitation of τ_3-$NiAl_3Ti_2$ from $\beta/B2$ phases occurred in Zone I, whereas only the phase transformation from α-Ti phase to α_2-Ti_3Al phase took place in Zone II. Conversely, the Ti/IN718 interface had more complex phase transformation and numerous diffusion zones. The diffusion bonding mechanism of Ti/IN718 interface is schematically shown in Fig. 12. At the initial stage of diffusion bonding, higher porosity existed at Ti/IN718 interface due to the presence of surface roughness, as shown in Fig. 12(a). As the temperature increased, due to substantial plastic deformation that occurred as a result of applied pressure, most areas at Ti/IN718 interface were in closer contact. Consequently, the atoms were able to diffuse between Ti interlayer and IN718 alloy, as shown in Fig. 12(b). During the subsequent solid-state phase transition, δ-$NiTi_2$ and η-Ni_3Ti phases were first formed at Ti/IN718 interface due to the nucleation of these phases

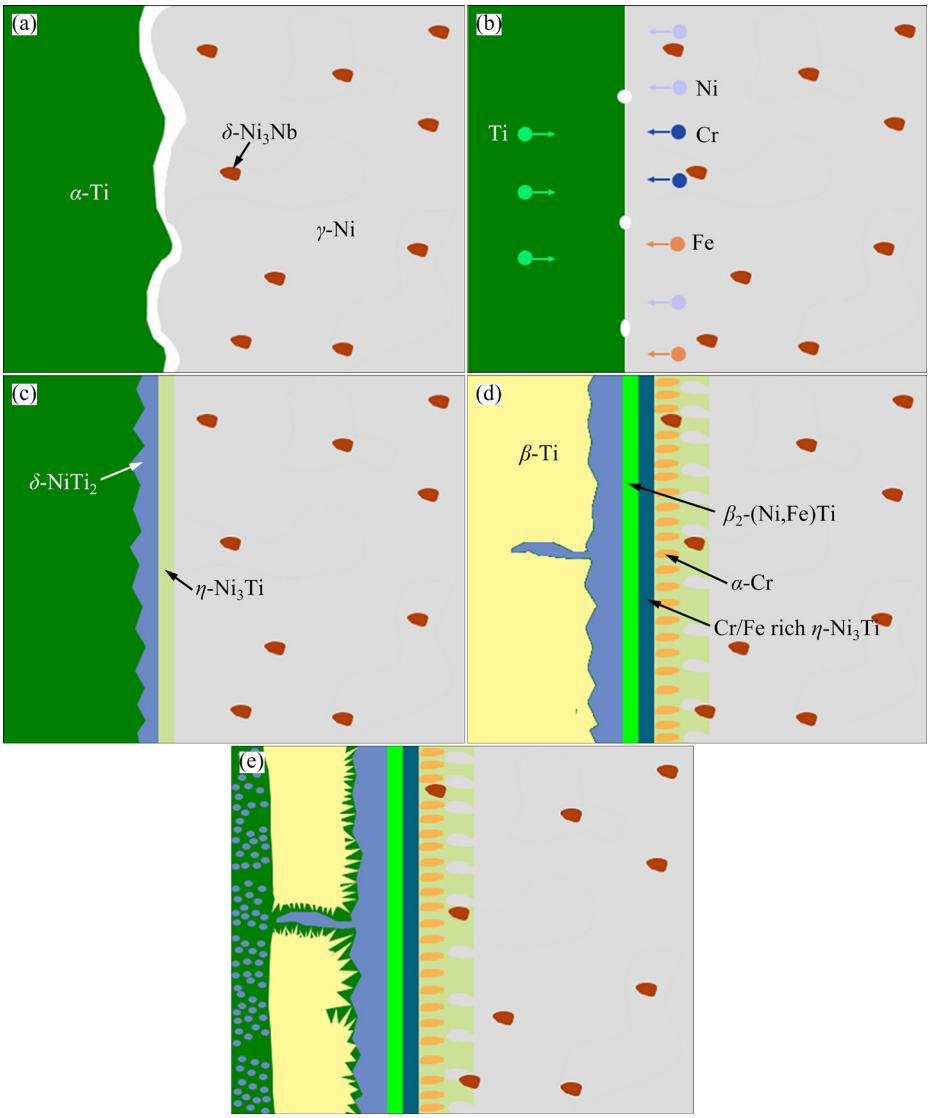

Fig. 12 Diagrams of diffusion bonding mechanism of Ti/IN718 interface: (a) Original interface; (b) Physical contact; (c) Formation of δ-$NiTi_2$ and η-Ni_3Ti phases; (d) Formation of β_2-(Ni,Fe)Ti, Cr/Fe-rich η-Ni_3Ti and α-Cr phases; (e) Formation of needle-like α-Ti phase and eutectoid microstructure (δ-$NiTi_2$+α-Ti)

occurring earlier than that of the NiTi phase [26,29], as shown in Fig. 12(c). During the holding process, α-Ti phase started to transform into β-Ti phase, facilitated by the diffusion of β-phase stabilizing elements Ni, Fe and Cr. Concurrently, a portion of δ-$NiTi_2$ phase grew along the grain boundaries of β-Ti phase due to the faster diffusion rate of Ni atoms in β-Ti phase [30]. In addition, the β_2-(Ni,Fe)Ti phase was formed between δ-$NiTi_2$ and η-Ni_3Ti phases. However, β_2 phase exerted a hindering effect on the diffusion of Cr and Fe atoms with a greater hindering effect on Cr. Consequently, during the subsequent diffusion bonding process, the Cr/Fe-rich η-Ni_3Ti and α-Cr phases were formed, as shown in Fig. 12(d). During the cooling process, β-Ti phase adjacent to δ-$NiTi_2$ phase transformed into needle-like α-Ti phase, and β-Ti phase close to the HNBG alloy side transformed into the eutectoid microstructure (δ-$NiTi_2$ + α-Ti). β-Ti phase in the remaining region was retained until room temperature, as shown in Fig. 12(e).

3.5 Fracture mechanism and mechanical properties of HNBG/Ti/IN718 joint

Figure 13 illustrates the nano-hardness test results of HNBG/Ti/IN718 joint produced at 850 °C, 20 min and 10 MPa. It can be observed that the hardness of Zones IV and (VI+VII) was higher than that of Zone V. This phenomenon can be attributed to the fact that the hardness of Ti−Ni intermetallic compounds follows in the decreasing order of δ-$NiTi_2$ > η-Ni_3Ti > β_2-NiTi. The higher hardness and elastic modulus of diffusion zones (VI+VII) may be related to the existence of higher density phase boundaries and grain boundaries. Due to the distribution of δ-$NiTi_2$ phase and the solution strengthening of Ni, Fe, Cr and Nb elements, the hardness and elastic modulus of Zone III were close to those of γ-TiAl phase.

Figure 14 illustrates the shear strength of HNBG/Ti/IN718 joints produced at different bonding parameters. The shear strength tended to first increase and then decrease with rising bonding temperature and time. Notably, the impact of the

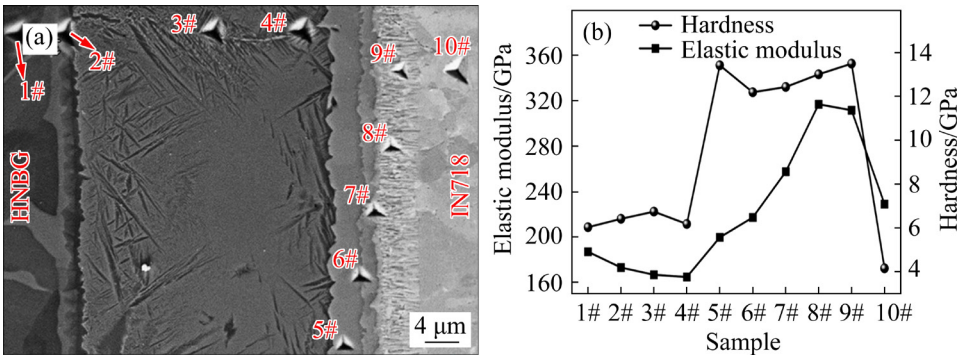

Fig. 13 Nano-indentation morphology (a) and hardness and elastic modulus distribution (b) of HNBG/Ti/IN718 joint produced at 850 °C, 20 min and 10 MPa

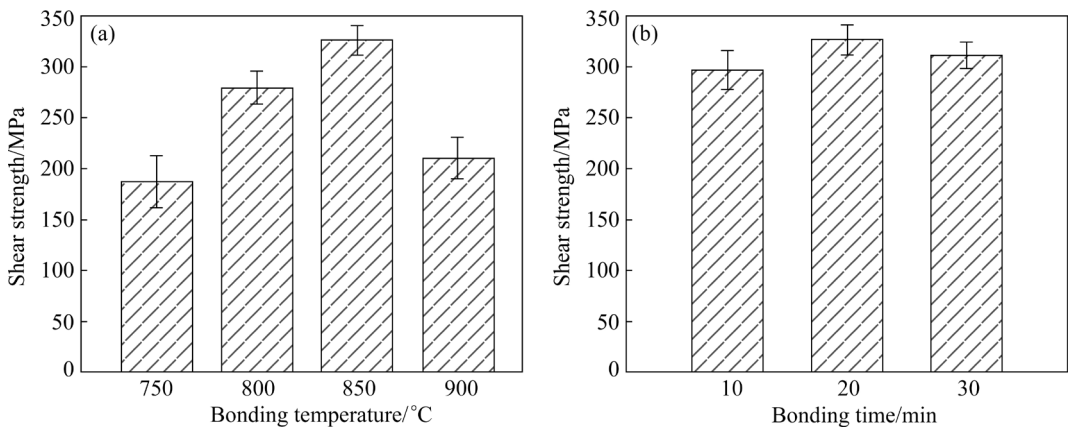

Fig. 14 Shear strength of HNBG/Ti/IN718 joints produced at different bonding parameters: (a) Bonding temperature; (b) Bonding time

temperature on shear strength outweighed that of time. When the bonding parameters were 850 °C, 20 min and 10 MPa, the shear strength of HNBG/Ti/IN718 joint reached the maximum of 326 MPa. In our previous research, the maximum shear strength of HNBG/IN718 joint was 257 MPa, and the corresponding joint was produced through direct diffusion bonding without any interlayer at 850 °C, 20 min and 10 MPa [19]. This suggests that the introduction of Ti interlayer could contribute to strengthening the bonding strength.

Figure 15 shows the shear fracture path of HNBG/Ti/IN718 joints produced at different bonding temperatures. It can be observed that the fracture mainly occurred along the interface between Zones IV and V at 750 °C, and a few cracks also appeared in Zone IV. According to the above analysis, the gaps and voids were present at the interface between Zones IV and V at lower bonding temperatures. This resulted in a high susceptibility to crack initiation and propagation. As the temperature increased, the gaps and voids gradually disappeared, enhancing the bonding strength of interface between Zones IV and V. Meanwhile, as the temperature increased, a larger number of δ-$NiTi_2$ phases with higher brittleness were formed in Zone IV. Consequently, crack propagation gradually shifted from the interface between Zones IV and V to the interior of Zone IV with increasing the bonding temperature.

Figure 16 illustrates the shear fracture morphology of HNBG/Ti/IN718 joints produced at different bonding temperatures. When the temperature was 750 °C, the fracture surface displayed a step-like morphology, as shown in Fig. 16(a). It can be observed from Fig. 16(b) that there existed a larger range of smooth areas and the cleavage steps between the smooth areas. Consequently, the fracture mode was brittle fracture along the phase interface and brittle cleavage fracture. Based on EDS result of Spot 2 in Table 3, δ-$NiTi_2$ phase was inferred to correspond to the fracture surface. As the temperature increased to 900 °C, the fracture surface displayed a ridge-like appearance, as shown in Fig. 16(c). It can be observed from Fig. 16(d) that there existed river patterns and cleavage steps. Consequently, the main fracture mode was cleavage fracture. Similarly, EDS result of Spot 2 in Table 3 indicated that δ-$NiTi_2$ phase corresponded to the fracture surface.

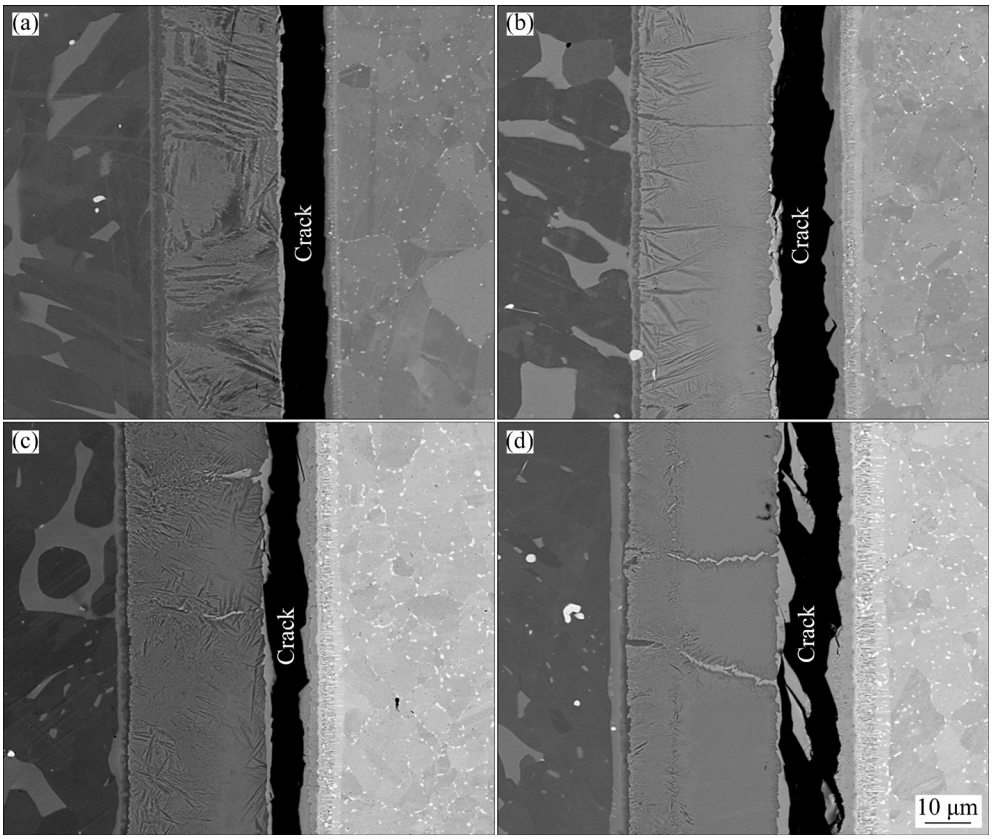

Fig. 15 Shear fracture path of HNBG/Ti/IN718 joints produced at different bonding temperatures: (a) 750 °C; (b) 800 °C; (c) 850 °C; (d) 900 °C

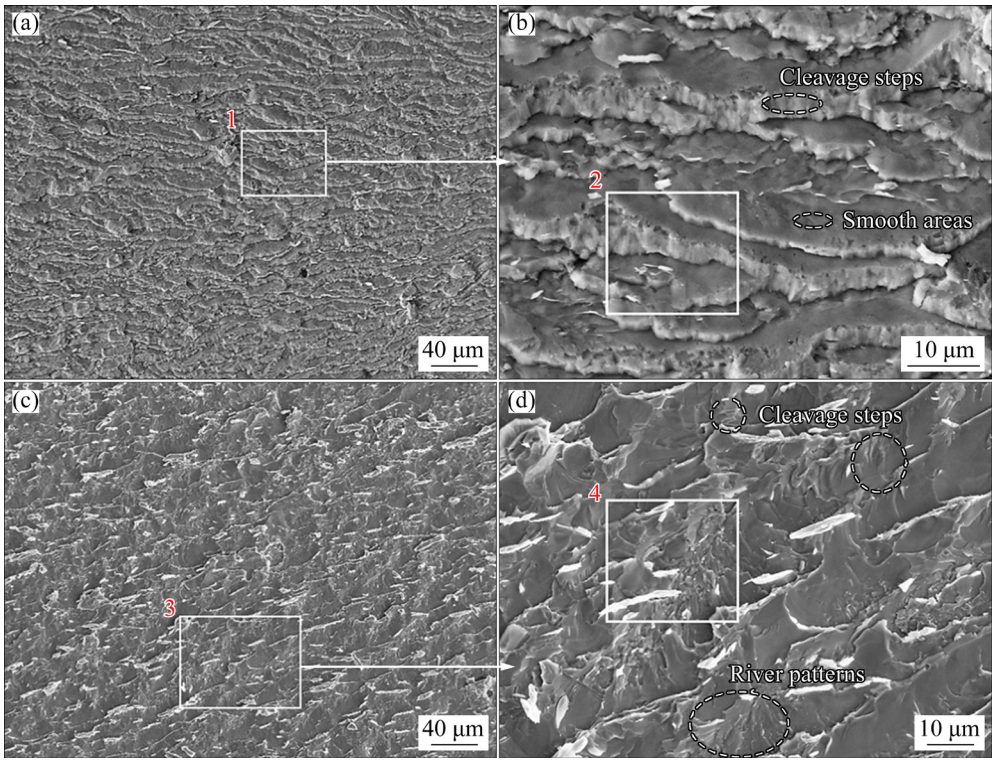

Fig. 16 Shear fracture morphology of HNBG/Ti/IN718 joints at different bonding temperatures: (a) 750 °C; (b) Local enlarged image of (a); (c) 900 °C; (d) Local enlarged image of (c)

Table 3 Element contents at spots marked in Fig. 16 detected by EDS

Spot	Content/at.%							Possible phase
	Ti	Al	Ni	Cr	Fe	Nb	Mn	
2	73.91	0.88	29.57	1.01	3.68	0.33	0.35	δ-$NiTi_2$
4	68.51	0.85	25.58	1.27	3.36	0.22	0.21	δ-$NiTi_2$

4 Conclusions

(1) The typical microstructure of HNBG/Ti/IN718 joint was HNBG//β/$B2$, τ_3-$NiAl_3Ti_2$//α_2-Ti_3Al//α-Ti+δ-$NiTi_2$, β-Ti//δ-$NiTi_2$//β_2-(Ni,Fe)Ti//Cr/Fe-rich η-Ni_3Ti, η-Ni_3Ti, α-Cr, δ-Ni_3Nb//η-Ni_3Ti, γ-Ni, δ-Ni_3Nb//IN718. The introduction of Ti interlayer significantly reduced the formation of brittle Ti−Ni−Al intermetallics.

(2) The segregation mechanism of Cr, Fe and Nb elements was that NiTi phase obstructed their diffusion.

(3) Gaps and Kirkendall voids gradually disappeared with increasing temperature. The defect-free joint was achieved at 850 °C. Unlike other zones, Zone II had a unique characteristic in that its thickness decreased steadily as the temperature increased. The amount of β-Ti phases in Ti interlayer increased with increasing the temperature.

(4) The bonding mechanism of Ti/IN718 interface was as follows. Initially, the physical contact of the interface was achieved by the action of temperature and pressure. Then, δ-$NiTi_2$ and η-Ni_3Ti phases were formed at IN718/Ti interface. During the heat preservation stage, β-Ti, β_2-(Ni,Fe)Ti, α-Cr and Cr/Fe-rich η-Ni_3Ti phases were formed, respectively. Finally, during the cooling stage, the portion of β-Ti phases transformed into α-Ti phases and eutectoid microstructure (δ-$NiTi_2$ + α-Ti), respectively. The remaining β-Ti phases were retained until room temperature.

(5) The shear strength of HNBG/Ti/IN718 joint tended to increase and then decrease with increasing the bonding temperature and time. The

maximum shear strength of HNBG/Ti/IN718 joint was 326 MPa, and the corresponding bonding parameters were 850 °C, 20 min and 10 MPa. At the bonding temperature of 750 °C, the fracture mainly occurred along the interface between Zones IV and V and the fracture mode was brittle fracture. When the bonding temperature was 900 °C, the fracture primarily occurred in Zone IV and the fracture mode was brittle cleavage fracture.

CRediT authorship contribution statement

Lai-qi ZHANG: Conceptualization, Methodology, Funding acquisition, Supervision; **Kun HE:** Data curation, Writing – Original draft, Writing – Review & editing; **Qiang GAO:** Investigation, Data curation, Writing – Review & editing.

Declaration of competing interest

The authors declare that they have no known competing financial interests or personal relationships that could have appeared to influence the work reported in this paper.

Acknowledgments

This work was supported by the National Natural Science Foundation of China (Nos. 52071021, 51871012), Beijing Natural Science Foundation, China (No. 2162024), the Fundamental Research Funds for the Central Universities, China (No. FRF-GF-20-20B), and the National Program on Key Basic Research Project of China (No. 2011CB605502).

References

[1] LI Xiao-bing, XU Hao, XING Wei-wei, CHEN Bo, SHU Lei, ZHANG Meng-shu, LIU Kui. Microstructural evolution and mechanical properties of forged β-solidified γ-TiAl alloy by different heat treatments [J]. Transactions of Nonferrous Metals Society of China, 2022, 32: 2229−2242.

[2] XU Run-run, LI Miao-quan, ZHAO Yong-hao. A review of microstructure control and mechanical performance optimization of γ-TiAl alloys [J]. Journal of Alloys and Compounds, 2023, 932: 167611.

[3] CLEMENS H, MAYER S. Design, processing, microstructure, properties, and applications of advanced intermetallic TiAl alloys [J]. Advanced Engineering Materials, 2013, 15: 191−215.

[4] WU Xin-hua. Review of alloy and process development of TiAl alloys [J]. Intermetallics, 2006, 14: 1114−1122.

[5] APPEL F, OEHRING M, PAUL J D H. Nano-scale design of TiAl alloys based on β-phase decomposition [J]. Advanced Engineering Materials, 2006, 8: 371−376.

[6] GE Geng-wu, WANG Ze-ming, LIANG Si-yuan, ZHANG Lai-qi. Achievement of forging without canning for β-solidifying γ-TiAl alloy containing high content of niobium [J]. Materials and Manufacturing Processes, 2021, 36: 1667−1676.

[7] XI Nai-yuan, TANG Ke-xin, FANG Xue-wei, LI Yan, DUAN Yu-song, HUANG Ke. Enhanced comprehensive properties of directed energy deposited Inconel 718 by a novel integrated deposition strategy [J]. Journal of Materials Science & Technology, 2023, 141: 42−55.

[8] YIN Qing-an, LIU Zhan-qiang, WANG Bing, SONG Qing-hua, CAI Yu-kui. Recent progress of machinability and surface integrity for mechanical machining Inconel 718: A review [J]. The International Journal of Advanced Manufacturing Technology, 2020, 109: 215−245.

[9] SONAR T, BALASUBRAMANIAN V, MALARVIZHI S, VENKATESWARAN T, SIVAKUMAR D. An overview on welding of Inconel 718 alloy—Effect of welding processes on microstructural evolution and mechanical properties of joints [J]. Materials Characterization, 2021, 174: 110997.

[10] CHEN Guo-qing, ZHANG Bing-gang, LIU Wei, FENG Ji-cai. Crack formation and control upon the electron beam welding of TiAl-based alloys [J]. Intermetallics, 2011, 19: 1857−1863.

[11] CAI Xiao-long, SUN Da-qian, LI Hong-mei, MENG Chao, WANG Lin, SHEN Cheng-jie. Dissimilar joining of TiAl alloy and Ni-based superalloy by laser welding technology using V/Cu composite interlayer [J]. Optics & Laser Technology, 2019, 111: 205−213.

[12] SEQUEIROS E W, GUEDES A, PINTO A M P, VIEIRA M F, VIANA F. Microstructure and strength of γ-TiAl alloy/Inconel 718 brazed joints [J] Materials Science Forum, 2012, 730: 835−840.

[13] REN Hai-shui, XIONG Hua-ping, LONG Wei-min, SHEN Yuan-xun, PANG Shu-jie, CHEN Bo, CHEN Yao-yong. Interfacial diffusion reactions and mechanical properties of Ti_3Al/Ni-based superalloy joints brazed with AgCuPd filler metal [J]. Materials Characterization, 2018, 144: 316−324.

[14] DONG Duo, SHI Kang-qiao, ZHU Dong-dong, LIANG Yong-feng, WANG Xiao-hong, WEI Zun-jie, LIN Jun-pin. Microstructure evolution and mechanical properties of high Nb–TiAl alloy/GH4169 joints brazed using CuTiZrNi amorphous filler alloy [J]. Intermetallics, 2021, 139: 107351.

[15] LI Hai-xin, HE Peng, LIN Tie-song, PAN Feng, FENG Ji-cai, HUANG Yu-dong. Microstructure and shear strength of reactive brazing joints of TiAl/Ni-based alloy [J]. Transactions of Nonferrous Metals Society of China, 2012, 22(2): 324−329.

[16] RAMOS A S, VIEIRA M T, SIMÕES S, VIANA F, VIEIRA M F. Joining of superalloys to intermetallics using nanolayers [J]. Advanced Materials Research, 2008, 59: 225−229.

[17] LUO Gen-xiang, WU Guo-qing, HUANG Zheng, RUAN Zhong-jian. Diffusion bonding of laser-surface-modified gamma titanium aluminide alloy to nickel-base casting alloy [J]. Scripta Materialia, 2007, 57: 521−524.

[18] LI Zi-fu, WU Guo-qing, HUANG Zheng, RUAN Zhong-jian. Diffusion bonding of laser surface modified TiAl alloy/Ni alloy [J]. Materials Letters, 2004, 58: 3470−3473.

[19] GAO Qiang, ZHANG Lai-qi, LIU Ji-yao, LIN Jun-pin. Microstructure and mechanical properties of high niobium β-γ TiAl and IN718 alloy joints diffusion bonded by spark plasma sintering [J]. Intermetallics, 2022, 151: 107745.

[20] GAO Qiang, WANG Ze-ming, ZHANG Lai-qi, GE Geng-wu. Joining of β-γ TiAl alloys containing high content of niobium by pulse current diffusion bonding [J]. Intermetallics, 2021, 133: 107184.

[21] SERVANT C, ANSARA I. Thermodynamic modelling of the order-disorder transformation of the orthorhombic phase of the Al−Nb−Ti system [J]. Calphad, 2001, 25: 509−525.

[22] DONG Hong-gang, YANG Zhong-lin, YANG Guo-shun, DONG Chuang. Vacuum brazing of TiAl alloy to 40Cr steel with $Ti_{60}Ni_{22}Cu_{10}Zr_8$ alloy foil as filler metal [J]. Materials Science and Engineering: A, 2013, 561: 252−258.

[23] CAO Jian, LIU Jia-kun, SONG Xiao-guo, LIN Xing-tao, FENG Ji-cai. Diffusion bonding of TiAl intermetallic and Ti_3AlC_2 ceramic: Interfacial microstructure and joining properties [J]. Materials & Design, 2014, 56: 115−121.

[24] SIMÕES S, TAVARES C J, GUEDES A. Joining of γ-TiAl alloy to Ni-based superalloy using Ag−Cu sputtered coated Ti brazing filler foil [J]. Metals, 2018, 8: 723.

[25] CAO Jian, GUO Xia-jun, SI Xiao-qing, LI Chun, LIU Jia-kun, QI Jun-lei, FENG Ji-cai. Evolution and formation mechanism of the interfacial microstructure on diffusion bonded joints of single crystal Ni-based superalloys to Ti_3AlC_2 ceramic with Ni interlayer [J]. Vacuum, 2021, 185: 110027.

[26] SHAO Xi, GUO Xiang-long, HAN Yuan-fei, LIN Zheng-jie, QIN Ji-ning, LU Wei-jie, ZHANG Di. Preparation of TiNi films by diffusion technology and the study of the formation sequence of the intermetallics in Ti–Ni systems [J]. Journal of Materials Research, 2014, 29: 2707−2716.

[27] SHEN Jing-yuan, HU Lian-xi, ZHANG Ling-yu, LIU Wen-chao, FANG Ai-wei, SUN Yu. Synthesis of TiAl/Nb composites with concurrently enhanced strength and plasticity by powder metallurgy [J]. Materials Science and Engineering: A, 2020, 795: 139997.

[28] LI Hai-xin, WEI Hong-mei, HE Peng, LIN Tie-song, FENG Ji-cai, HUANG Yu-dong. Effects of alloying elements in GH99 superalloy on microstructure evolution of reactive brazing TiAl/GH99 joints [J]. Intermetallics, 2013, 34: 69−74.

[29] BASTIN G F, RIECK G D. Diffusion in the titanium-nickel system: I. Occurrence and growth of the various intermetallic compounds [J]. Metallurgical Transactions, 1974, 5: 1817−1826.

[30] GIBBS G B, GRAHAM D, TOMLIN D H. Diffusion in titanium and titanium—niobium alloys [J]. Philosophical Magazine, 1963, 8: 1269−1282.

高铌 β/γ-TiAl 与 Ni 基高温合金加钛中间层的脉冲电流扩散连接

张来启[1]，贺 昆[1]，高 强[1,2]

1. 北京科技大学 新金属材料全国重点实验室，北京 100083；
2. 鞍钢集团 北京研究院有限公司 钒钛研究院分院，北京 102209

摘 要：以纯钛箔为中间层，采用脉冲电流对高铌 β/γ-TiAl 金属间化合物(HNBG)和镍基高温合金(IN718)进行扩散连接。对 HNBG/Ti/IN718 接头的显微组织、元素偏析及力学性能进行研究，并探讨钛中间层对接头显微组织和力学性能的影响。HNBG/Ti/IN718 接头的典型显微组织为 HNBG//$\beta/B2$，τ_3-$NiAl_3Ti_2$//α_2-Ti_3Al//α-Ti+δ-$NiTi_2$，β-Ti//δ-$NiTi_2$//β_2-(Ni,Fe)Ti//Cr/富 Fe η-Ni_3Ti，η-Ni_3Ti，α-Cr，δ-Ni_3Nb//η-Ni_3Ti，γ-Ni，δ-Ni_3Nb//IN718。随着连接温度的升高，间隙和柯肯达尔孔洞逐渐消失。Cr、Fe 和 Nb 元素偏析的机制是 β_2-NiTi 相阻碍了它们的扩散。纳米压痕结果表明，位于 IN718 合金一侧的扩散区硬度较高。在连接参数为 850 ℃、20 min 和 10 MPa 的条件下，接头剪切强度达到最大值 326 MPa。断裂发生在 IV 区和 V 区，断裂模式为脆性断裂和解理断裂。钛中间层的引入改善了接头显微组织，增强了结合强度。

关键词：高铌 β/γ-TiAl 金属间化合物；IN718 合金；钛中间层；扩散连接；显微组织；力学性能；元素偏析

(Edited by Wei-ping CHEN)